UCLA
UCLA Previously Published Works

Title

Determination of dose rate effects on Zircaloy oxidation using proton irradiation and oxygen transport modeling

Permalink

https://escholarship.org/uc/item/89g7p5cv

Authors

Reyes, Michael
Wang, Peng
Was, Gary
et al.

Publication Date

2019-09-01

DOI

10.1016/j.jnucmat.2019.05.039

Peer reviewed

eScholarship.org Powered by the California Digital Library
University of California

Journal of Nuclear Materials 523 (2019) 56–65

Contents lists available at ScienceDirect

Journal of Nuclear Materials

journal homepage: www.elsevier.com/locate/jnucmat

Determination of dose rate effects on Zircaloy oxidation using proton irradiation and oxygen transport modeling

Michael Reyes [a], Peng Wang [b], Gary Was [b], Jaime Marian [a, c, *]

[a] Department of Mechanical and Aerospace Engineering, University of California Los Angeles, Los Angeles, CA, 90095, USA
[b] Nuclear Engineering and Radiological Sciences, University of Michigan, Ann Arbor, MI, 48109, USA
[c] Department of Materials Science and Engineering, University of California Los Angeles, Los Angeles, CA, 90095, USA

ARTICLE INFO

Article history:
Received 19 November 2018
Received in revised form
20 May 2019
Accepted 20 May 2019
Available online 27 May 2019

Keywords:
Zirconium oxide
Zircalloy clad
Zircalloy corrosion
Oxidation
Nuclear reactor

ABSTRACT

While much of our knowledge about zirconium corrosion at high temperatures comes from out-of-pile experiments performed over the last several decades, understanding the behavior of Zr clad in light water reactor (LWR) conditions requires studying corrosion acceleration under irradiation. In-pile tests are slow and costly to perform, and only allow limited flexibility when it comes to exploring key parameters such as dose, dose rate, temperature, and alloy composition. In contrast, proton irradiations provide a good match for LWR dose rates and for the spatial uniformity of neutron irradiation, and thus constitute a very robust experimental platform from which to explore these parameters. In this work, we present an extension of a recently proposed Zr oxidation kinetic model that accounts for acceleration of oxide layer growth due to irradiation, accompanied by a set of controlled experiments carried out in a corrosion loop coupled to an accelerator beam line for parameterization and validation. The model includes radiation enhanced diffusion (RED) of oxygen in the oxide as the main effect of irradiation, and uses the experimental results of oxide layer growth as a function of dose rate to parameterize the RED coefficients. We show that these coefficients are strongly dose rate-dependent, which is quantitatively consistent with a negligible effect of RED on corrosion acceleration in the pre-transition regimes of samples irradiated under LWR conditions. We also find a smooth transition from columnar to equiaxed oxide grain growth as the proton irradiation dose rate increases.

© 2019 Elsevier B.V. All rights reserved.

1. Introduction

Understanding the behavior of nuclear-grade Zr alloy fuel clad under irradiation is key to the safe and reliable operation of light-water reactors (LWR) in nuclear power plants. Corrosion of the cladding has been extensively documented, both under in- and out-of-pile conditions [1–9], although the majority of our understanding comes from controlled autoclave and corrosion loop experiments without irradiation in various Zr-based alloys going back several decades [10–15]. Reactor experiments are costly to perform due to irradiated specimen handling, low dose rates, and number of variables implicated. However, from the limited in-pile database available on Zr-metal clad, it is known that neutron exposure accelerates corrosion compared to the unirradiated case [2,5–7,16]. As well, irradiation is seen to fundamentally alter microstructure evolution during the growth of the oxide scale in Zr alloys [5,16–18]. However, due to the complex corrosion kinetics associated with LWR conditions, it is difficult to use in-pile data to separate the effect of the different reactor variables (temperature, neutron dose and dose rate, water chemistry, alloy composition, spatial variations, etc) on the material response. Alternatives to in-pile studies have been proposed, generally based on a combination of exposure to high temperature water and controlled charged-particle irradiations [19–21], exploiting the advantageous properties of ion beams for these types of studies [22–24]. For example, Woo et al. have carried out *ex situ* tests consisting of exposing pre-irradiated Zircaloy-2 to high temperature water followed by electron irradiation of the pre-corroded alloy [25]. Xu et al. inverted the order by irradiating Zircaloy-4 specimens with Ar ions and subsequently exposing them to sulfuric acid at room temperature [26]. Bererd et al. have studied Zr oxidation *in-situ* under Xe-ion irradiation to mimic the effect of irradiation of fission products

* Corresponding author. Department of Materials Science and Engineering, University of California Los Angeles, CA 90095, USA.
E-mail address: jmarian@ucla.edu (J. Marian).

https://doi.org/10.1016/j.jnucmat.2019.05.039
0022-3115/© 2019 Elsevier B.V. All rights reserved.

originating in the fuel side [27]. Unfortunately, while ion-irradiation studies provide easy control of irradiation variables, their quantitative potential is typically constrained by low material penetration and high irradiation dose rate. More recently, Wang and Was have taken advantage of the unique properties of proton irradiation to mimic neutron damage [28] to study corrosion effects in implanted Zircaloy-4 samples [18]. They have carried out *in situ* tests in a specially-designed corrosion loop at temperatures of 310°C. This modified loop allows modification of key experimental variables such as water temperature, chemistry, and flow speed, as well as irradiation dose and dose rate [29].

While it is clear that irradiation of Zr alloys accelerates corrosion in-pile, the mechanisms behind such behavior are yet not clear. Radiation enhanced diffusion (RED) is a well understood phenomenon in which excess point defects produced by irradiation couple to matrix or solute atoms, speeding up their motion through the lattice. Oxygen ion transport is a natural RED candidate as it proceeds via a vacancy mechanism that is highly susceptible to the defect concentration. However, no convincing evidence has been found of the accumulation of point defects in ZrO_2 [4,7,14] or other features that would suggest an enhanced defect production. Another aspect not clarified to date is how pre- and post-transition kinetics are affected by irradiation. The evidence in some cases suggests that only the post-transition regime is influenced [31–33], consistent with the notion that no RED is observed in the oxide during its initial growth period. However, recent studies paint the inverse picture, with an apparent corrosion acceleration during the pre-transition stage [18]. Note that in this paper the term 'transition' is used to refer to the first instance observed experimentally when the kinetics appears to change from that described by a power law in time, while the oxide acts as a protective layer, to that when this protectiveness is lost. Finally, radiolysis is also known to be enhanced by irradiation [17,30,34–36], generally resulting in an accelerated corrosion rate by way of an increased concentration of oxidizing species in the water.

An essential aspect of the investigation of oxidation kinetics during irradiation is developing reliable models. Phenomenological models assuming *a priori* power law kinetics to match experimental observations have been developed over the years [31,37–40]. These models predict power law pre-transition behavior (whether it is 1/2 or 1/3 time scaling) by design and therefore add little to our fundamental understanding of the oxidation process. Approaches that are formulated starting from fundamental transport equations and interface physics have subsequently been developed [41–45], shedding light on issues such as the role of electron transport, effects of charge distributions, transition from 1/2 to 1/3 time kinetics, etc. Extension to irradiation conditions has been undertaken typically using empirical correlations linking oxide growth to burnup [37,40,41]. While these models can yield good quantitative estimates of oxide thickness growth in a variety of conditions, they do not help us answer any of the fundamental questions raised above.

In this paper, we present a numerical/experimental study of Zircaloy-4 oxidation consisting of proton irradiation experiments as a function of dose rate on specimens in a corrosion loop exposed to water at 320°C, and an extension of the kinetic oxidation model presented in Ref. [45] that incorporates RED during the pre-transition stage. The model is calibrated with the experimental data, yielding the values of the radiation-enhanced diffusion coefficient as a function of dose rate. The paper is organized as follows. Next, we discuss the phenomenology of the oxidation kinetics of Zircaloy-4. Then, we describe the implementation of the RED extension into the kinetic model, as well as the experimental apparatus and conditions. We then extract the RED coefficient by fitting the model to the experimental data points and discuss the evolution of the alloy microstructure. We conclude with a discussion of the results and their significance for understanding irradiation effects in laboratory irradiation experiments. While we focus on the behavior of Zr oxide under irradiation, it is worth noting that irradiation damage in the substrate metal α-Zr has also been extensively studied and documented [46–50].

2. Methods

2.1. Phenomenology of oxide growth during irradiation

In out-of-pile conditions, the oxygen ions available from the reduction of water at the clad's outer surface penetrate in the Zr matrix via diffusion. As the oxygen concentration builds up, the resulting Zr–O mixtures evolve through different phases, including solid solutions and intermetallics. As the O:Zr atom ratio reaches the values of the different line compounds predicted by the phase diagram, i.e. 2:1 corresponding to Zr_2O, 1:1 for the δ'-ZrO phase, and 1:2 for ZrO_2, well-defined interfaces appear, with clear jumps in the stoichiometric oxygen concentration across each of them [51,52]. Analyses of these phases using advanced characterization techniques suggest very slow oxygen diffusivity through the Zr_2O and ZrO layers, consistent with strong stoichiometric compounds with very low vacancy concentrations. This is substantiated by their very small thicknesses (on the order of several tens of nm) compared to the micron-level thickness of the ZrO_2 passivating layer [12,51,53].

Interestingly, the existence of these suboxide phases appears to be incompatible with the formation of a region near the oxide/metal interface of tetragonal zirconia (denoted β-ZrO_2) [54–56], although the reasons for this are not clear. While β-ZrO_2 exists as a high-temperature phase of Zr oxide, it is known to be stabilized at reactor temperaturtes by Pilling-Bedworth stresses originating from the lattice mismatch at the interface (1.56 for Zr alloys). As well, tetragonal ZrO_2 is seen to form under slight nonstoichiometric conditions, as $ZrO_{(2-x)}$ with $x < 0.02$ [57,58]. The substoichiometric nature of this tetragonal zirconia region is essential to understanding the growth kinetics of the oxide layer as a whole, as the extra oxygen vacancies result in an excess concentration of holes that leads to the formation of a charge gradient near the interface [44]. In our previous paper describing the chemical reaction kinetic model, we have shown that this charge gradient creates a drift for oxygen diffusion, leading to the peculiar $t^{1/3}$ dependence of the oxide growth law in Zr alloys [45]. Away from the interface, ZrO_2 exists as a strong line compound in the monoclinic phase (α-ZrO_2). The oxide scale grows in the form of elongated (columnar) grains aligned with the radial direction, with the exception of the local tetragonal layer, where grains are seen to be smaller and more equiaxed [59,60].

Irradiation fundamentally changes this picture by introducing vacancies homogeneously across the oxide scale and weakening the charge gradients. Oxygen transport is then seen to proceed more uniformly, leading to microstructures that tend to be dominated by more irregular grains without a clear directionality [12,59–62]. Other key effects of irradiation in Zr alloys are the amorphization and dissolution (not always connected) of Cr and Fe-containing precipitates, which is known to accelerate the corrosion kinetics in the post-transition regime, at least in PWR primary water [7,63–67]. The cause of this is thought to be related to an enhanced Fe solute concentration (otherwise trapped in Zr–Fe intermetallics), as alloys without Fe have been observed to display lower corrosion rates when subjected to similar environments [7]. Another factor to keep in mind for in-pile conditions is an enhanced production of radicals from water molecules due to radiolysis. However, by far the main effect of ionizing radiation on

water chemistry has been shown to be the heightened production of hydrogen (either as a single species or attached to water molecules as H_2O_2), having only a moderate impact on O ion production [17,34,68,69], particularly in primary water where radiolysis is suppressed by hydrogen enrichment of the water.

In any case, our one-dimensional kinetic model does not capture these microstructural and chemical features, focusing instead on the growth of different layers as affected by enhanced oxygen diffusion. Here we further reduce the model by eliminating the ZrO layer due to its limited effect on the overall time evolution of the oxide layer, as has been shown in the literature [12,51,53], leading to a system defined only by the 'oxide' (β and α zirconia without distinction) and the 'metal' (including all suboxides and solid solutions). This approach is also consistent with recent observations of corrosion acceleration in Zircaloy-4 irradiation experiments where a sharp transition between the oxide film and the metal layer was seen [33].

2.2. Description of the kinetic model

A detailed description of the model, its implementation, numerical stability, and sensitivity to key parameters has been given by Reyes et al. [45] and here we give only a brief overview. We use a one-dimensional *Stefan* model to predict the evolution of the oxide/metal interface. This interface moves as a consequence of discontinuities in the oxygen flux resulting from diffusion in different media. The evolution of the interface, located at coordinate s, is described by the following equation of motion:

$$\dot{s} = \frac{J_{ox}}{2\rho_{Zr}} = -\frac{D_{ox}\nabla c_{ox}}{2\rho_{Zr}} \tag{1}$$

where J_{ox} is the mass flux, D_{ox} and c_{ox} are the oxygen diffusion coefficient and concentration in ZrO_2, respectively, and ρ_{Zr} is the atomic density of the metal. Determination of c_{ox} requires solving a general mass balance equation of the type:

$$\frac{\partial c_i}{\partial t} = \nabla(D_i\nabla c_i) + \frac{U_i D_i}{kT^2}\nabla c_i \nabla T + \frac{q_i D_i}{kT}\nabla(c_i\nabla\varphi) \tag{2}$$

also known as the *drift-diffusion* equation [70]. The i subindex refers to the oxide ('ox') or the metal ('m'). The three terms on the r.h.s. of the equation represent, respectively, *Fickian* diffusion, *thermomigration*, and *electro-migration*. D_i, U_i, and q_i are, respectively, the oxygen diffusivity, oxygen atom migration energy, and charge in each layer i. φ is the electrical potential, which must be determined separately solving a Poisson equation subjected to a fixed charge density of ρ_0 at the interface. T is the absolute temperature, and k Boltzmann's constant. Note that the diffusion coefficient is assumed to follow an Arrhenius form:

$$D_i(T) = D_i^0 \exp\left(-\frac{U_i}{kT}\right)$$

where D_i^0 is the corresponding diffusion prefactor.

Equation (2) can be further simplified by accounting for the particularities of each layer and the boundary conditions. In this work, we consider corrosion loops with constant water temperature, such that the thermomigration term can be neglected. Further, it is assumed that the metal layer is charge neutral and therefore eq. (2) reduces to a simple diffusion equation:

$$\frac{\partial c_m}{\partial t} = \nabla(D_m\nabla c_m) \tag{3}$$

For its part, the evolution equation in the oxide layer is written as:

$$\frac{\partial c_{ox}}{\partial t} = \nabla(D_{ox}\nabla c_i) + \frac{q_{ox}D_{ox}}{kT}\nabla(c_{ox}\nabla\varphi) \tag{4}$$

where it is assumed that a charge gradient develops due to an excess oxygen vacancy concentration at the interface associated with the formation of tetragonal ZrO_{2-x} [42,44,71,72]. A schematic depiction of the geometry considered in the model is shown in Fig. 1. Under irradiation, we adopt the standard form for the steady state *radiation enhanced diffusion* (RED) coefficient [73,74]:

$$D_{ox}^{rad} = D_{ox}\left(1 + a\dot{\phi}^b\right) = D_{ox}^0 \exp\left(-\frac{U_{ox}}{kT}\right)\left(1 + a\dot{\phi}^b\right) \tag{5}$$

where U_{ox} is the activation energy for oxygen migration, $\dot{\phi}$ is the dose rate, a is a constant, and b is an exponent that reflects the nature of irradiation defect recombination. When point defects recombine via correlated (or spontaneous) recombination, or when they annihilate predominantly at fixed sinks, the RED coefficient is independent of temperature, and it depends linearly on irradiation flux, $b = 1$. Conversely, when point defects annihilate by uncorrelated (diffusion mediated) recombination, $b = 1/2$ [74]. D_{ox}^{rad} replaces D_{ox} in eq. (4) under irradiation conditions.

Equations (3) and (4) are linked by the jump in the oxygen concentration at the interface, i.e.:

$$c_{ox}(s,t) = c_m(s,t) + 2\rho_{Zr}$$

where the term $2\rho_{Zr}$ reflects the stoichiometric concentration of oxygen in the oxide (twice the number of Zr atoms). Note that this is a *dynamic* boundary condition in the sense that it depends on s, which in turn depends on t. The system of equations (1)–(4) is closed by adding the following boundary conditions to the one just introduced:

$$c_m(x,0) = 0$$

$$c_{ox}(0,t) = C_0$$

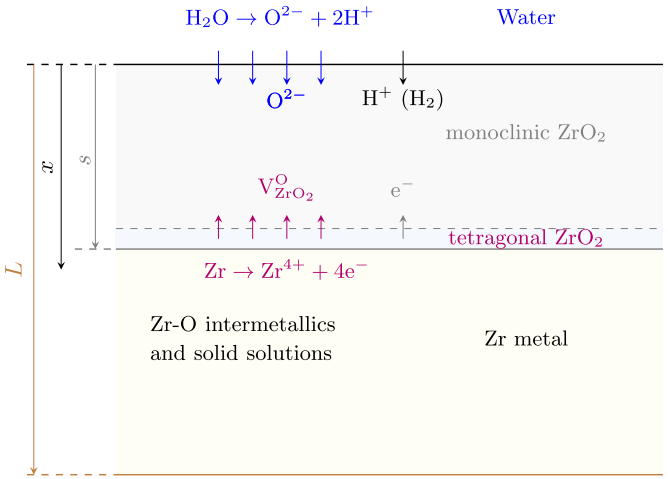

Fig. 1. Schematic diagram (not to scale) of the geometry considered in the corrosion model considered in this work. x is the depth variable, s is the thickness of the oxide layer, and L is the total thickness of the specimen. The chemical processes occurring at each interface are shown for reference.

$$\frac{\partial c_m(L,t)}{\partial y} = 0$$

with C_0 the free oxygen concentration in the coolant, and L the clad total thickness.

The above equations are valid during Stage 1, while the oxide layer grows maintaining its protective properties. However, as the oxidation process continues, microcracks developed in the oxide scale created by Pilling-Bedworth stresses grow, leading to porosity and providing enhanced avenues for O diffusion. This marks the beginning of Stage 2, where O transport is no longer the rate-limiting mechanism. Then, one uses the following evolution equation which replaces eq. (1):

$$\dot{s} = \frac{C_0 v}{2\rho_{Zr}} \tag{6}$$

where v is the velocity of the viscous flow of water through the crack network. Upon this transition, the boundary conditions switch to:

$$c_{ox}(x \le s, t > t_{1\to 2}) = c_m(s, t > t_{1\to 2}) = C_0$$

v sets the slope of the linear growth regime when $t > t_{1\to 2}$.

The time evolution of the oxide layer thickness in the pre-transition regime is ultimately fitted to an expression of the type:

$$s(t) = ct^n \tag{7}$$

where c and n are a prefactor and the growth exponent, respectively. The transition from Stage 1–2 appears to correlate very clearly with oxide thickness, suggesting that fragmentation occurs above a given stress threshold. This thickness, which we term s^*, is alloy-dependent but is seen to generally range between 1.0 and 2.5 μm [14]. Thus, the relationship between oxide growth and irradiation can be condensed into the following two points:

(i) As eq. (6) shows, the growth of the oxide layer during Stage 2 does not depend on irradiation dose (inasmuch as it does not depend on diffusion).
(ii) While irradiation dose is seen to have little effect on s^*, the time at which the transition occurs is accelerated with dose rate [18], as will be shown below.

2.3. Experimental

The purpose of the experiments was (i) to validate the irradiation-accelerated oxidation kinetic model and act as a platform for fitting some of its key parameters, and (ii) to study the effect of dose rate on oxide microstructure under dynamic conditions. To mimic operation conditions as closely as possible, the experimental samples were simultaneously exposed to high-temperature, high-pressure water (320°, 14 MPa) on one side, and proton irradiation from the backside of the sample (corresponding to high vacuum conditions, ~ 10^{-8} torr).

2.3.1. Specimen design and damage calculations

Proton irradiations were conducted at the Michigan Ion Beam Laboratory, using a proton beam accelerated to 5.4 MeV. To achieve the highest degree of spatial uniformity in the irradiation, the specimen thickness was designed to allow the proton beam to pass completely through and into the water as modeled using the SRIM program [75]. A 5.4-MeV proton has a range of 146 μm, so a sample thickness of 120 μm was chosen to ensure complete penetration by the proton beam. As a result, the damage peak lies in the water as shown in Fig. 2.

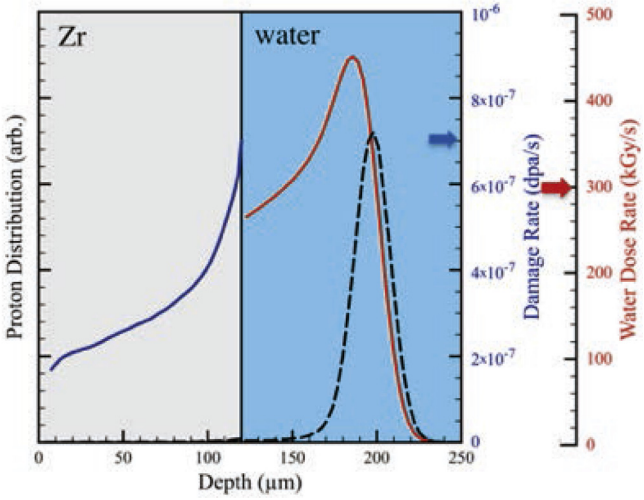

Fig. 2. SRIM simulated damage rate, atom deposition and water dose rate plot for a 120 μm Zr sample irradiated with 5.4 MeV protons at 320°C in water.

The irradiation of the water must be taken into consideration to account for radiolysis of corrosion species and their effect on oxidation kinetics. The proton beam deposits approximately 3.9 MeV in the Zr sample, and 1.5 MeV in the water. The range of the proton in the water was calculated to be approximately 100 μm at 320°C. Under a typical proton current density of 2 μA/cm^2, a damage rate at the metal/water interface of 7×10^{-7} dpa/s is calculated, leading to an energy deposition rate in the water of 340 kGy/s, as shown in Fig. 2 [1].

Energy deposited in the water is expended primarily in radiolysis of water molecules. Although there are several types of possible radiolytic species, H_2O_2 is known to be longest-lived and strongly affects the electrochemical corrosion potential. The G-value for hydrogen peroxide production at 320°C based on the model given by Elliot and Bartels [78] is $G(H_2O_2) = 0.4 \times 10^{-7}$ mol/J. The estimated molar concentration of hydrogen peroxide at our beam density of 2 μA/cm^2 is then 0.16 μM. As shown by Tachibana et al. [79], the corrosion potential for hydrogenated water is shifted from −600 mV_{SHE} (typical for simulated primary water conditions) to the range − 200-to-+100 mV_{SHE} at 0.16 μM (5 wt ppb) H_2O_2.

2.3.2. Beam operation and sample assembly

While raster-scanning an area of approximately 1 cm^2, the beam passes through a set of 6 × 6 mm slit openings, after which the beam thickness is further reduced by a 2-mm diameter circular tantalum aperture on the back of the sample mount. This is done to reduce the activation caused by high energy protons directly hitting the zirconium mount. An additional center hole 1.6 mm in diameter was machined in the sample mount to act as the final aperture for the beam to pass through and hit the specimen, while still being sufficiently small to allow the mount to support the foil, preventing any mechanical failure or deformation of the sample. The sample assembly consists of a flat foil sandwiched between the mount and the top washer, as shown in Fig. 3. The assembly was then welded at the perimeter of the sample using a pulse arc welder to create a watertight seal between the vacuum-facing side and water-facing side. After the welding process, each welded sample undergoes a

[1] Details on how to arrive at these numbers can be found in Refs. [76,77].

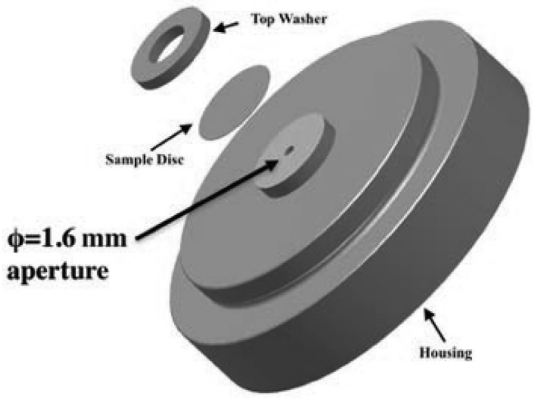

Fig. 3. Schematic diagram of the sample assembly.

high-pressure water leak test to ensure water tightness and mechanical integrity. No sample oxidation was observed after the welding process.

As shown in Fig. 4, the welded sample assembly is then loaded between the beam-line flange and the miniature corrosion cell. The high-pressure water seal was achieved by use of a pre-oxidized zirconium gasket, which deforms elastically when compressed between the cell and beam-line flange and is chemically stable when exposed to high-temperature water. The full vacuum seal was achieved by a soft copper gasket, which plastically deforms into the matching grooves.

2.3.3. Post-irradiation characterization

Post-irradiation characterization was carried out on the irradiated-corroded sample using focused ion beam (FIB) milling to prepare 100-nm-thick lamellas for transmission electron microscopy (TEM) analysis on a FEI Helios 650 nanolab SEM/FIB. The irradiated oxide thickness was measured and the oxide microstructure was characterized in bright field (BF) and high angle annular dark field (HAADF) mode using a JEOL 3100R05 scanning TEM (STEM).

2.4. Model parameterization

An exhaustive parameterization study was conducted in our previous work for pure Zr, Zircaloy-4, and Zr–Nb alloys [45]. Table 1 gives the values of the relevant material constants for unirradiated Zirc-4 used to solve eqs. (3) and (4) (with the source indicated in each case). These set the baseline behavior of the alloy, together with the values of L and T, which are set experimentally to 120 μm and 320°C. The permittivity used here was 3.26×10^{29} [$C^2 \cdot eV^{-1}$].

Here we fit the values of C_0 and ρ_0 such that the model predicts a Stage 1 → 2 transition precisely at a thickness of s^* and a time $t_{1\to2}$ for the unirradiated case, and then assume that these values remain constant under irradiation. This is intended to limit the effects of dose rate to the RED coefficient alone, and not muddle the global behavior by using multiple parameter dependences. We recognize that this might be a strong assumption in some cases. Beyond that, the numerical behavior of the model is discussed in detail in ref. [45]. The values of δt and δy employed here were obtained from numerical stability analyses for explicit finite difference discretizations of eq. (4), and were, respectively, 0.26 h and 0.16 μm.

3. Results

Fig. 5 shows oxide thickness measurements from *in-situ* irradiation corrosion experiments compared with in-pile data generated from MATPRO [82]. All experiments were conducted in miniature corrosion cells (as illustrated in Sec. 2.3) at 320°C, in pure water with 3 wt parts per million of dissolved hydrogen, for up to 54 days for the unirradiated exposure, and up to 72 h for the *in-situ* irradiation-corrosion experiments. The unirradiated oxide growth rate was in good agreement with out-of-pile data, while the results from the proton irradiation corrosion experiments reveal significantly higher growth rates, up to 13 times, than in the unirradiated case.

Next, we apply the model described in Sec. 2.2 with the parameters discussed in Sec. 2.4 to the conditions under which the experimental data from Fig. 5 were obtained. We have used the model previously for out-of-pile Zircaloy-4 with good success [45], and thus we use the same parameters (as given in Table 1), except the oxygen diffusivity, for which the RED model is now used (cf. Sec. 2.2). The results are provided in Fig. 6, where the experimental data points are shown along with the model curves for all irradiation dose rates considered. The values of c and n in eq. (7) for each dose rate are given in Table 2.

The shaded area in the figure corresponds to Stage 1 growth when the oxide acts as a protective layer, which ends after the oxide reaches a thickness of 2.0 μm. As mentioned above, we hypothesize that this threshold remains independent of irradiation dose rate, which follows from the conjecture that failure is primarily determined by the accumulation of Pilling-Bedworth stresses [45]. A feature not immediately evident from the experimental data is whether the post-transition growth rates above approximately

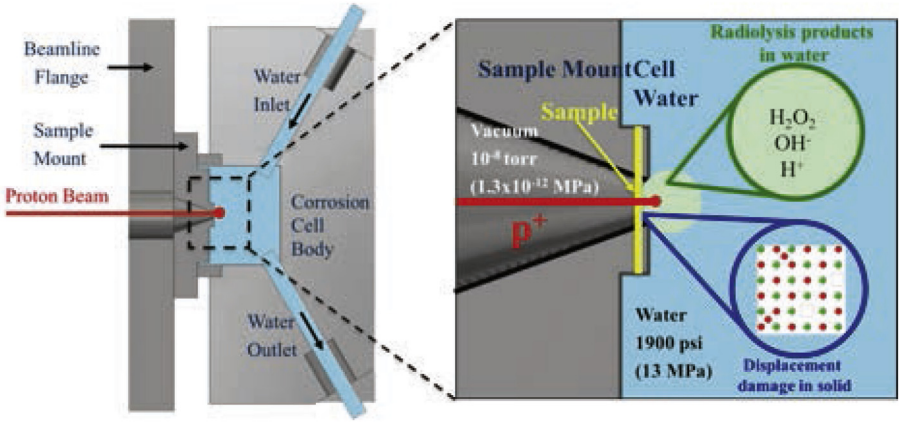

Fig. 4. Schematic representation of the miniature corrosion cell for the in-situ proton irradiation-corrosion experiment.

Table 1
Material constants for unirradiated Zircaloy-4 with the source indicated in each case.

s^* [μm]	$t_{1\to2}$ [days]	D_m^0 [$m_2 s^{-1}$]	U_m [eV]	D_{ox}^0 [$m^2 \cdot s^{-1}$]	U_{ox} [eV]	C_0 [ρ_{Zr}]	ρ_0 [$C \cdot m^{-2}$]
2.1 [18]	512 [18]	3.92×10^{-4}[80]	2.2 [80]	2.76×10^{-6}[81]	1.5 [81]	0.87	145.0

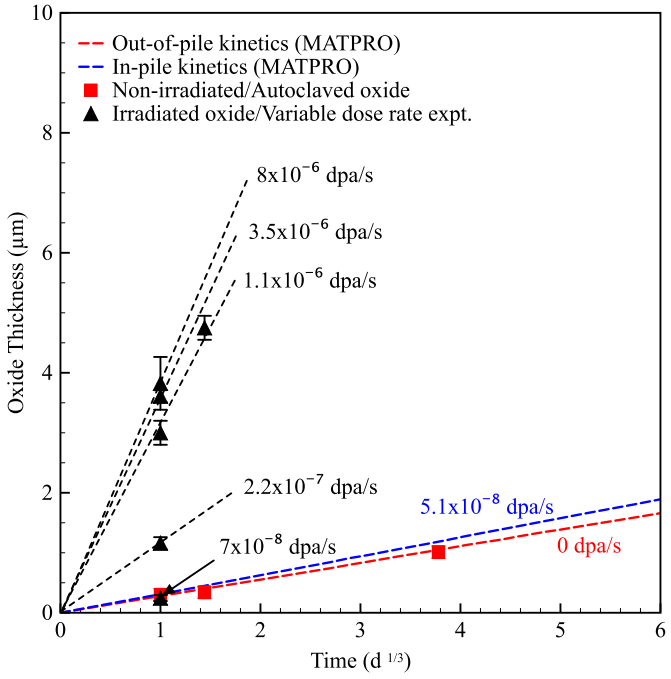

Fig. 5. Experimental measurements of the dependence of oxide layer thickness on damage rate.

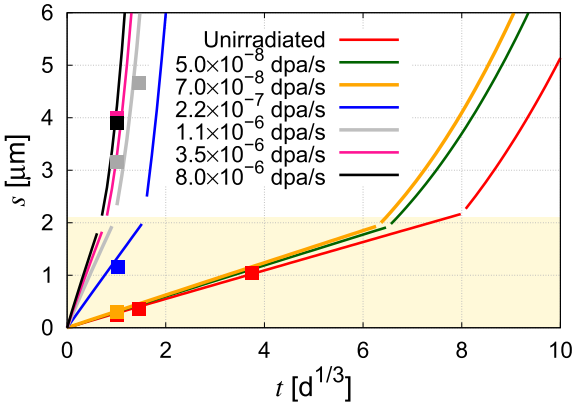

Fig. 6. Model predictions and associated experimental data (squares) as a function of dose rate.

Table 2
Coefficients of eq. (7) and RED coefficients (at 320°C) as a function of the proton irradiation rate.

Dose rate [dpa/s]	c	n	D_{ox}^{rad} [m^2/s]
0.0	0.28	0.33	4.7×10^{-20}
5.0×10^{-8}	0.30	0.33	6.4×10^{-20}
7.0×10^{-8}	0.31	0.33	7.0×10^{-20}
2.2×10^{-7}	1.31	0.33	4.8×10^{-18}
1.1×10^{-6}	2.12	0.32	2.1×10^{-17}
3.5×10^{-6}	2.55	0.32	3.7×10^{-17}
8.0×10^{-6}	2.91	0.32	5.7×10^{-17}

10^{-6} dpa$\cdot s^{-1}$ are insensitive to the proton irradiation rate. We will shed light on this issue below when the results are analyzed in the context of the experimental growth rates.

The RED coefficient can now be extracted from the results shown in Fig. 6 by mapping the model parameters to the RED coefficient in eq. (5). Fig. 7 shows the values at the different dose rates considered, from which the values of a and b can be extracted. Not shown in the range of the figure is the diffusivity for the unirradiated case, which is also used as a fitting point. The values of D_{ox}^{rad} at 320°C are also provided in Table 2.

Two analytical functions are plotted in Fig. 7, one bearing a 1/2 exponent and the other being linear. The coefficients a and b in eq. (5) are $a = 3.0 \times 10^{-14}$ and $b = 1/2$ for the blue curve, and $a = 4.9 \times 10^{-12}$, $b = 1$ for the red one (a in units of $m^2 \cdot$ dpa$\cdot s^{-2}$). The square-root dependence provides a reasonable fit to the data in the entire dose rate range, suggesting perhaps that irradiation defect accumulation is recombination-controlled for all dose rate experiments reported here. However, the high dose rate data points are also well represented by a linear law. Linear behavior is expected when damage accumulation is defect sink-controlled, which could be plausible in view of the microstructural changes that will be presented below. In other words, our data cannot conclusively establish the type of regime encountered in the experiments at the higher dose rates, as arguments for and against a linear law can be made. What can be said with more certainty is that the low dose rate results are consistent with a recombination-controlled behavior characterized by long-range diffusion and low sink densities. It must also be noted that eq. (5) has been found to work well in metals, but there is no evidence that it should also in ceramics as in this case.

Finally, we study the growth rate of the oxide scale, comparing model predictions to experimental mass gain measurements, which are done for Zirc-4 specimens containing 3 ppm of H_2 at 320°C. Our predictions are obtained by differentiating eq. (7) with respect to time and calculating the resulting values at 24 h of exposure, consistent with experimental conditions:

$$\dot{s}(t, \dot{\phi}) = cnt^{n-1}|_{\dot{\phi}}$$

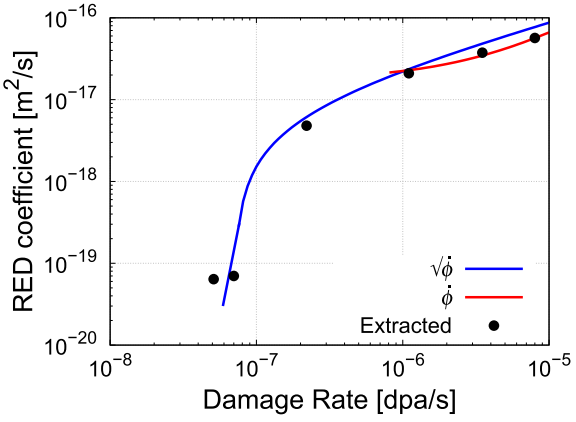

Fig. 7. Variation of the radiation enhanced diffusivity (RED) with dose rate and fits to two RED models based on eq. (5). (For interpretation of the references to colour in this figure legend, the reader is referred to the Web version of this article.)

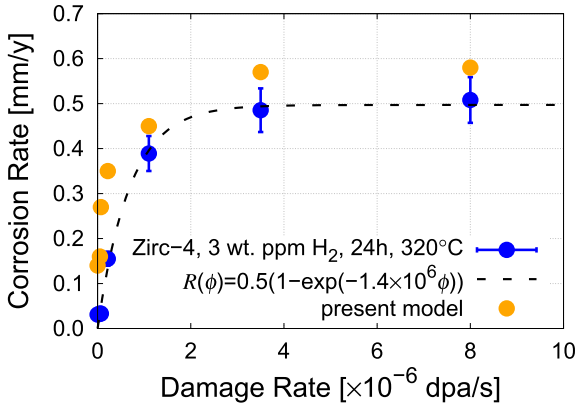

Fig. 8. Oxide scale growth rate as a function of dose rate. The graph shows the experimental results (of Zircaloy-4 exposed to irradiation for 24 h in pure water with 3 wt ppm dissolved H_2 at a temperature of 320°C), an exponential fit to the measurements (denoted by $R(\dot{\phi})$), and predictions from the present model.

The results are given in Fig. 8, where good agreement is found between the model predictions and the experimental data. In actuality, this represents an internal consistency check, as the model predictions themselves at each dose rate derive from oxide layer thickness measurements (in Fig. 6). It is worth noting that the corrosion rates shown in the figure for the higher damage rates are significantly higher those found in-reactor corrosion. This is not surprising in light of the fact that the corrosion kinetics is always fastest at the beginning, and our data points are all in the first 24-h period. More importantly, our corrosion rates at reactor-equivalent dose rates match well with those found in LWR conditions.

In any case, an important determination can now be inferred from the figure: the saturation of the growth rate with irradiation dose rate suggests that in all experiments carried out above $\dot{\phi} \gtrsim 3 \sim 4\times10^{-6}$ dpa·s^{-1}, oxide growth is insensitive to irradiation rate. Since it was established earlier that breakaway growth (Stage 2) occurs at the same rate irrespective of dose rate, this behavior suggests that tests done in this regime result in almost no discernible transition between Stages 1 and 2.

3.1. Evolution of the microstructure with dose rate

There are two fundamental questions relating irradiation to the microstructure of the oxide. The first is the shape of the grains. It is well known that the oxide actually forms by way of nucleation and growth of grains that grow into the metal. The manner in which they grow, however, can be noticeably different with and without irradiation[2]. It is believed that oxygen diffusion through the oxide —on its way to the oxide/metal interface— proceeds along grain boundaries, which provide enhanced avenues for atomic transport compared to the interior of the grain [83,84]. Compressive Pilling-Bedworth stresses are known to assist in this mechanism by neutralizing diffusion along the hoop direction. This directionality may be behind the observation of long columnar grains forming the oxide layer in out-of-pile conditions, both for Zircaloy-2 and 4 [12,62,85–87]. Under irradiation, the emergence of RED, with excess vacancies supplying extra oxygen transport inside the grains, helps relax the compressive stresses in the oxide. This naturally results in less elongated, more equiaxed grains in the case of irradiation. Nucleation is another key factor that influences grain morphology. The enhanced oxygen transport brought about by RED during irradiation can also accelerate the nucleation rate, and so long as damage is produced more or less uniformly within the oxide, this results in smaller grains undergoing isotropic growth.

The role of dose rate, then, would be to provide a transition from columnar growth to equiaxed grains, with importance shifting from growth to nucleation. This is indeed confirmed in our characterization of the oxide microstructures presented in Fig. 9. The figure clearly illustrates the transition from elongated to equiaxed grain shapes as the irradiation dose rate increases. The images correspond to exposures of 24 h, which puts these microstructures mostly in the pre-transition stage.

The second microstructural aspect is the stability of monoclinic Zr oxide under irradiation. Recent work points to modifications in the volume fraction of the tetragonal ZrO_2 phase with irradiation dose and dose rate, which is generally seen to increase. Monoclinic ZrO_2 has been observed to transform into the tetragonal (as well as cubic) phase in controlled Xe ion irradiations to 2 dpa of fluence at temperatures as low as 120 K [88]. The effect has also been seen under Ni-ion irradiations at 323 K [89]. While equiaxed grains of tetragonal ZrO_2 are routinely seen in contact with the α-Zr matrix in out-of-pile conditions [58], this evidence points to an interdispersion of these grains in the monoclinic layer under irradiation. Whether this is a transformation to the tetragonal phase of existing monoclinic grains or simply a retention of grains formed under compressive stresses at the interface [90] is not clear, and our characterization does not provide any additional evidence at this moment.

4. Discussion

On the experimental side, the main finding of this paper is that irradiation dose rate has a strong effect on corrosion kinetics. From a qualitative point of view, this is consistent with a scenario governed by radiation enhanced diffusion, which supplies excess vacancies that accelerate oxygen transport in the oxide. In metals, RED manifests itself in two clearly differentiated forms: (i) as a square root dependence of the oxygen diffusion coefficient on irradiation dose rate at low values of $\dot{\phi}$, and (ii) a linear dependence at higher dose rates. While it is not clear that the same scalings can be applied to ceramics, here our goal is to simply use a well-established model of RED and evaluate its applicability to Zr oxide. The existence of different scalings can be correlated with a gradual transformation of the microstructure from large directional grains increasingly towards smaller, equiaxed grains as the dose rate is increased. However, our analysis of the diffusivities at each rate shown in Fig. 7 cannot conclusively establish this presupposition, as a curve with a 1/2 exponent —i.e. irradiation damage controlled by defect recombination— suffices to fit the data in the entire dose rate range. We are led then to conclude that we do not have a sufficient amount of data to ascertain whether such a transition exists.

The question still remains as to how to reconcile the present results with recent and past in-reactor experiments which lead to different observations. For example, Kammezind et al. [33] have carried out irradiations of Zircaloy-4 specimens in PWR conditions (temperatures between 270 and 350°C, fluxes of 10^{14} (fast, >1 MeV) neutrons per cm^2 per second). They observed that the radiation environment had little effect on the pre-transition corrosion rates, up to fluences on the order of 10^{22} neutrons per cm^2, indicating that neutron damage had no effect on the oxide layer itself. Instead, TEM examinations revealed that irradiation was seen to impact only the underlying base metal. Similar conclusions were reached in other studies carried out in PWR

[2] While this is a generally accepted observation, it does not always apply to corrosion films obtained under light water reactor irradiation conditions.

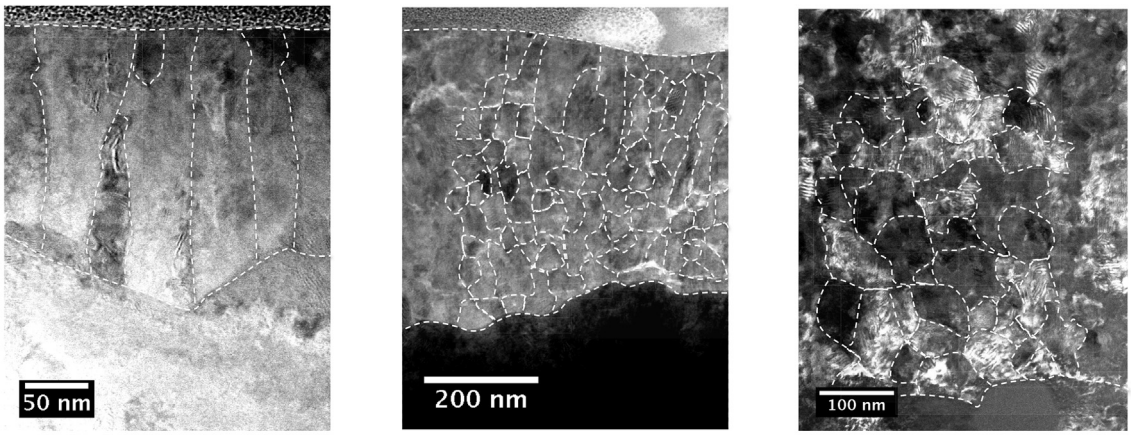

(a) 7.0×10^{-8} dpa·s^{-1} (b) 2.2×10^{-7} dpa·s^{-1} (c) 3.5×10^{-6} dpa·s^{-1}

Fig. 9. Damage rate dependence on microstructural evolution, clearly showing a transition with dose rate from columnar to equiaxed grain growth. The environment side is at the top of the figures.

conditions [31]. In general, the observed microstructures in these tests consisted primarily of columnar monoclinic grains elongated in the growth direction of the oxide layer, with an interspersed distribution of smaller and more equiaxed grains within the columnar structure. Interestingly, this is the type of microstructure observed at low dose rates in our experiments. As Fig. 9a shows, at dose rates below 10^{-7} dpa/s, the oxide layer is composed of mostly large columnar grains, much like those observed in PWR irradiations. Indeed, representative (fast neutron) dose rates at ATR and HFIR[3] are on the order 10^{-7} dpa/s [91].

Therefore, we are led to surmise the existence of a shift at a threshold dose rate between a regime where damage is seen to have little effect on the pre-transition corrosion kinetics but significant alterations to the post-transition kinetics (up to 30 × in some cases [33]), and one characterized by the inverse —i.e. strong impact on pre-transition and little or no effect on the post-transition behavior. This would correspond to a fundamental transformation of the microstructure from a long columnar grain structure to a smaller equiaxed structure. In turn, this could potentially indicate a situation where irradiation damage is controlled by uncorrelated defect recombination shifting to one controlled by correlated recombination (square root dependence on dose rate of the RED coefficient) or, alternatively, defect absorption at grain boundary sinks (linear dependence).

At any rate, our data do not conclusively support that the mechanisms observed here may also be representative of LWR (primary water) experiments. Our argument then is that either (i) the low dose rates typical of light-water reactor conditions are not sufficient to push the oxide layer microstructure through this presumed transition, or (ii) our results are not extrapolable in a meaningful way to reactor conditions. However, our results systematically varying the ion irradiation dose rate are the first to capture this behavior, revealing a new regime where corrosion of Zircaloy (and possibly other derivative alloys) is accelerated during Stage 1.

5. Conclusions

We end this paper with a list of the most important conclusions:

- Systematic proton irradiations of Zircaloy-4 in an especially-designed corrosion loop have been carried out at dose rates between 5×10^{-8} and 8×10^{-6} dpa•s^{-1} and a temperature of 320°C. The experiments show an acceleration of corrosion rate of the samples with dose rate, with the growth rate gradually flattening as the dose rate increases.
- A kinetic model of oxide scale formation and growth in Zircaloy under irradiation that tracks the motion of the oxide/metal interface governed by oxygen diffusion has been developed. The model includes concentration driven transport, thermo-migration, and electro-migration.
- The model is parameterized with both experimental and computational data. The RED coefficient is directly fitted to the experimental data obtained in this work.
- The model accounts for irradiation by replacing the diffusivity of oxygen in ZrO_2 with a radiation enhanced diffusion coefficient that depends on the irradiation dose rate. The scaling of the RED coefficient with the irradiation dose rate follows a square root scaling at the lower dose rates, while at higher dose rates we do not have sufficient information to decisively establish the scaling displayed by the data.
- Our results show that at dose rates characteristic of light water power reactors, RED is not a significant corrosion-enhancing mechanism, in agreement with corrosion data for Zircaloy-4 in LWR conditions.

Acknowledgments

This research was supported by the Consortium for Advanced Simulation of Light Water Reactors (CASL), an Energy Innovation Hub for Modeling and Simulation of Nuclear Reactors under U.S. Department of Energy Contract No. DE-AC05-00OR22725. Helpful discussions with A. Couet, A. Motta, B. D. Wirth, and A. Van der Ven are acknowledged.

Appendix A. Supplementary data

Supplementary data to this article can be found online at https://doi.org/10.1016/j.jnucmat.2019.05.039.

References

[1] G.H. Jenks, Review and Correlation of In-Pile Zircaloy-2 Corrosion Data and a Model for the Effect of Irradiation, Tech. Rep., Oak Ridge National Lab., Tenn.,

[3] The *Advanced Test Reactor* and the *High-Flux Isotope Reactor*, the primary experimental neutron irradiation facilities in the US.

1961.
[2] O. Gebhardt, Investigation of in-pile formed corrosion films on zircaloy fuel rod claddings by impedance spectroscopy and galvanostatic anodization, J. Nucl. Mater. 203 (1) (1993) 17–26.
[3] F. Garzarolli, H. Stehle, E. Steinberg, Behavior and properties of zircaloys in power reactors: a short review of pertinent aspects in lwr fuel, in: Zirconium in the Nuclear Industry: Eleventh International Symposium, ASTM International, 1996.
[4] Y.H. Jeong, B. Baek, S. Park, et al., Waterside Corrosion of Zirconium Alloys in Nuclear Power Plants, Tech. Rep., Korea Atomic Energy Research Institute, 1999.
[5] P. Rudling, G. Wikmark, A unified model of zircaloy bwr corrosion and hydriding mechanisms, J. Nucl. Mater. 265 (1–2) (1999) 44–59.
[6] P. Bossis, J. Thomazet, F. Lefebvre, Study of the mechanisms controlling the oxide growth under irradiation: characterization of irradiated zircaloy-4 and zr-1nb-o oxide scales, in: Zirconium in the Nuclear Industry: Thirteenth International Symposium, ASTM International, 2002.
[7] B. Cox, Some thoughts on the mechanisms of in-reactor corrosion of zirconium alloys, J. Nucl. Mater. 336 (2–3) (2005) 331–368.
[8] Y.H. Jeong, S.-Y. Park, M.-H. Lee, B.-K. Choi, J.-H. Baek, J.-Y. Park, J.-H. Kim, H.-G. Kim, Out-of-pile and in-pile performance of advanced zirconium alloys (hana) for high burn-up fuel, J. Nucl. Sci. Technol. 43 (9) (2006) 977–983.
[9] M. Preuss, P. Frankel, S. Lozano-Perez, D. Hudson, E. Polatidis, N. Ni, J. Wei, C. English, S. Storer, K. Chong, et al., Studies regarding corrosion mechanisms in zirconium alloys, in: Zirconium in the Nuclear Industry: 16th International Symposium, ASTM International, 2012.
[10] S. Kass, The development of the zircaloys, in: Corrosion of Zirconium Alloys, ASTM International, 1964.
[11] E. Hillner, Corrosion of zirconium-base alloys: an overview, in: Zirconium in the Nuclear Industry, ASTM International, 1977.
[12] A. Garner, A. Gholinia, P. Frankel, M. Gass, I. MacLaren, M. Preuss, The microstructure and microtexture of zirconium oxide films studied by transmission electron backscatter diffraction and automated crystal orientation mapping with transmission electron microscopy, Acta Mater. 80 (2014) 159–171.
[13] T. Allen, R. Konings, A. Motta, 5.03 corrosion of zirconium alloys, Comprehensive nuclear materials, 2012, pp. 49–68.
[14] A.T. Motta, A. Couet, R.J. Comstock, Corrosion of zirconium alloys used for nuclear fuel cladding, Annu. Rev. Mater. Res. 45 (2015) 311–343.
[15] A.T. Motta, A. Couet, R.J. Comstock, Corrosion of zirconium alloys used for nuclear fuel cladding, Annu. Rev. Mater. Res. 45 (1) (2015) 311–343, https://doi.org/10.1146/annurev-matsci-070214-020951, arXiv: https://doi.org/10.1146/annurev-matsci-070214-020951.
[16] F. Garzarolli, E. Steinberg, H.G. Weidinger, Microstructure and corrosion studies for optimized pwr and bwr zircaloy cladding, in: Zirconium in the Nuclear Industry: Eighth International Symposium, ASTM International, 1989.
[17] B. Cox, Effects of irradiation on the oxidation of zirconium alloys in high temperature aqueous environments: a review, J. Nucl. Mater. 28 (1) (1968) 1–47.
[18] P. Wang, G.S. Was, Oxidation of zircaloy-4 during in situ proton irradiation and corrosion in pwr primary water, J. Mater. Res. 30 (9) (2015) 1335–1348.
[19] J.A. Spitznagel, L.R. Fleischer, W.J. Choyke, The Effects of Ion Bombardment on the Thin Film Oxidation Behavior of Zircaloy-4 and Zr-1.0 Nb, Springer US, Boston, MA, 1974, pp. 87–99, https://doi.org/10.1007/978-1-4684-2079-1_7. https://doi.org/10.1007/978-1-4684-2079-1_7.
[20] C. Yan, R. Wang, Y. Wang, X. Wang, G. Bai, Effects of ion irradiation on microstructure and properties of zirconium alloys: a review, Nucl. Eng. Technol. 47 (3) (2015) 323–331. https://doi.org/10.1016/j.net.2014.12.015. http://www.sciencedirect.com/science/article/pii/S1738573315000170.
[21] S. Hua-Hai, P. Shu-Ming, Z. Xiao-Song, S. Kai, W. Lu-Ming, Z. Xiao-Tao, Microstructure evolution of zircaloy-4 during ne ion irradiation and annealing: an in situ tem investigation, Chin. Phys. B 23 (3) (2014), 036102. http://stacks.iop.org/1674-1056/23/i=3/a=036102.
[22] G.S. Was, T.R. Allen, Radiation damage from different particle types, in: Radiation Effects in Solids, Springer, 2007, pp. 65–98.
[23] M.J. Fluss, P. Hosemann, J. Marian, Charged-particle irradiation for neutron radiation damage studies, Char. Mater. (2012) 1–17.
[24] S. Zinkle, L. Snead, Opportunities and limitations for ion beams in radiation effects studies: bridging critical gaps between charged particle and neutron irradiations, Scripta Mater. 143 (2018) 154–160.
[25] O.T. Woo, G. McDougall, R.M. Hutcheon, V. Urbanic, M. Griffiths, C.E. Coleman, Corrosion of electron-irradiated zr-2.5 nb and zircaloy-2, in: Zirconium in the Nuclear Industry: Twelfth International Symposium, ASTM International, 2000.
[26] J. Xu, X. Bai, F. He, S. Wang, X. He, Y. Fan, Influence of ar ion bombardment on the uniform corrosion resistance of laser-surface-melted zircaloy-41 financed by institute of low energy nuclear physics, radiation beam and materials laboratory, beijing normal university.1, J. Nucl. Mater. 265 (3) (1999) 240–244. https://doi.org/10.1016/S0022-3115(98)00732-6. http://www.sciencedirect.com/science/article/pii/S0022311598007326.
[27] N. Bérerd, A. Chevarier, N. Moncoffre, H. Jaffrézic, E. Balanzat, H. Catalette, Zirconium oxidation under high-energy heavy-ion irradiation, J. Appl. Phys. 97 (8) (2005), 083528.
[28] G.S. Was, Challenges to the use of ion irradiation for emulating reactor irradiation, J. Mater. Res. 30 (9) (2015) 1158–1182.
[29] S.S. Raiman, A. Flick, O. Toader, P. Wang, N.A. Samad, Z. Jiao, G.S. Was, A facility for studying irradiation accelerated corrosion in high temperature water, J. Nucl. Mater. 451 (1–3) (2014) 40–47.
[30] O. Woo, G. McDougall, R. Hutchinson, V. Urbanic, M. Griffiths, C. Coleman, Tech. rep.
[31] B. Cheng, P. Gilmore, H. Klepfer, PWR Zircaloy Fuel Cladding Corrosion Performance, Mechanisms, and Modeling, 1996.
[32] D. Gilbon, B. Bonin, Les combustible nucleaires, Tech. rep. (2008).
[33] B. Kammenzind, J. Gruber, R. Bajaj, J. Smee, Neutron irradiation effects on the corrosion of zircaloy-4 in a pressurized water reactor environment, in: Zirconium in the Nuclear Industry: 18thInternational Symposium, ASTM International, 2018.
[34] W. Burns, P. Moore, Water radiolysis and its effect upon in-reactor zircaloy corrosion, Radiat. Eff. 30 (4) (1976) 233–242.
[35] F. Lefebvre, C. Lemaignan, Irradiation effects on corrosion of zirconium alloy claddings, J. Nucl. Mater. 248 (1997) 268–274.
[36] C. Sun, R. Hui, W. Qu, S. Yick, Progress in corrosion resistant materials for supercritical water reactors, Corros. Sci. 51 (11) (2009) 2508–2523.
[37] P. Billot, A. Giordano, Comparison of zircaloy corrosion models from the evaluation of in-reactor and out-of-pile loop performance, in: Zirconium in the Nuclear Industry: Ninth International Symposium, ASTM International, 1991.
[38] B. Cox, Modelling the corrosion of zirconium alloys in nuclear reactors cooled by high temperature water, in: Modelling Aqueous Corrosion, Springer, 1994, pp. 183–200.
[39] O. Coindreau, C. Duriez, S. Ederli, Air oxidation of zircaloy-4 in the 600-1000c temperature range: Modeling for astec code application, J. Nucl. Mater. 405 (3) (2010) 207–215. https://doi.org/10.1016/j.jnucmat.2010.07.038. http://www.sciencedirect.com/science/article/pii/S002231151000348X.
[40] V. Bouineau, A. Ambard, G. Bénier, D. Pêcheur, J. Godlewski, L. Fayette, T. Duverneix, A new model to predict the oxidation kinetics of zirconium alloys in a pressurized water reactor, in: Zirconium in the Nuclear Industry: 15th International Symposium, ASTM International, 2009.
[41] A.I.A. Almarshad, A. Klein, A model for waterside oxidation of zircaloy fuel cladding in pressurized water reactors, J. Nucl. Mater. 183 (3) (1991) 186–194.
[42] Review of theoretical conceptions on regimes of oxidation and hydrogen pickup in Zr-alloys.
[43] P. Gondi, G.F. Missigolli, Electron microscope observations on the oxidation of zirconium. a contribution to the cubic kinetic theory, Il Nuovo Cimento XL VIII B (2) (1967) 223–236.
[44] A. Couet, A.T. Motta, A. Ambard, The coupled current charge compensation model for zirconium alloy fuel cladding oxidation: I. parabolic oxidation of zirconium alloys, Corros. Sci. 100 (2015) 73–84. http://doi.org/10.1016/j.corsci.2015.07.003. http://www.sciencedirect.com/science/article/pii/S0010938X15300019.
[45] M. Reyes, A. Aryanfar, S.W. Baek, J. Marian, Multilayer interface tracking model of zirconium clad oxidation, J. Nucl. Mater. 509 (2018) 550–565. https://doi.org/10.1016/j.jnucmat.2018.07.025. http://www.sciencedirect.com/science/article/pii/S0022311517318317.
[46] G. Hood, R. Schultz, J. Jackman, Recovery of Single Crystal. Cap alpha.-zr from Low Temperature Electron Irradiation. A Positron Annihilation Spectroscopy Study.
[47] R. Holt, Mechanisms of irradiation growth of alpha-zirconium alloys, J. Nucl. Mater. 159 (1988) 310–338.
[48] S. Wooding, L. Howe, F. Gao, A. Calder, D. Bacon, A molecular dynamics study of high-energy displacement cascades in α-zirconium, J. Nucl. Mater. 254 (2–3) (1998) 191–204.
[49] A. Garde, G. Smith, R. Pirek, In-pwr irradiation performance of dilute tin-zirconium advanced alloys, in: Zirconium in the Nuclear Industry: Thirteenth International Symposium, ASTM International, 2002.
[50] S.I. Choi, J.H. Kim, Radiation-induced dislocation and growth behavior of zirconium and zirconium alloys–a review, Nucl. Eng. Technol. 45 (3) (2013) 385–392.
[51] Y. Dong, A.T. Motta, E.A. Marquis, Atom probe tomography study of alloying element distributions in zr alloys and their oxides, J. Nucl. Mater. 442 (1) (2013) 270–281.
[52] B. Puchala, A. Van der Ven, Thermodynamics of the zr-o system from first-principles calculations, Phys. Rev. B 88 (2013), 094108.
[53] K.J. Annand, I. MacLaren, M. Gass, Utilising dual eels to probe the nanoscale mechanisms of the corrosion of zircaloy-4 in 350c pressurised water, J. Nucl. Mater. 465 (2015) 390–399. https://doi.org/10.1016/j.jnucmat.2015.06.022. http://www.sciencedirect.com/science/article/pii/S0022311515300477.
[54] Corrosion of Zirconium Alloys in Nuclear Power Plants, Tech. Rep. IAEA-TECDOC-684, International Atomic Energy Agency, 1993.
[55] P. Platt, P. Frankel, M. Gass, R. Howells, M. Preuss, Finite element analysis of the tetragonal to monoclinic phase transformation during oxidation of zirconium alloys, J. Nucl. Mater. 454 (1) (2014) 290–297. https://doi.org/10.1016/j.jnucmat.2014.08.020. http://www.sciencedirect.com/science/article/pii/S0022311514005480.
[56] A.T. Motta, A. Couet, R.J. Comstock, Corrosion of zirconium alloys used for nuclear fuel cladding, Annu. Rev. Mater. Res. 45 (1) (2015) 311–343.
[57] J.P. Abriata, J. Garcés, The o-zr (oxygen-xirconium) system, Bulletin of Alloy Phase Diagrams 7 (2) (1986) 116–124.
[58] N. Ni, D. Hudson, J. Wei, P. Wang, S. Lozano-Perez, G. Smith, J. Sykes,

S. Yardley, K. Moore, S. Lyon, R. Cottis, M. Preuss, C. Grovenor, How the crystallography and nanoscale chemistry of the metal/oxide interface develops during the aqueous oxidation of zirconium cladding alloys, Acta Mater. 60 (20) (2012) 7132–7149. https://doi.org/10.1016/j.actamat.2012.09.021. http://www.sciencedirect.com/science/article/pii/S1359645412006441.

[59] B. Wadman, Z. Lai, H. Andren, A. Nyström, P. Rudling, H. Pettersson, Microstructure of oxide layers formed during autoclave testing of zirconium alloys, in: Zirconium in the Nuclear Industry: Tenth International Symposium, ASTM International, 1994.

[60] W. Qin, C. Nam, H. Li, J. Szpunar, Tetragonal phase stability in zro2 film formed on zirconium alloys and its effects on corrosion resistance, Acta Mater. 55 (5) (2007) 1695–1701.

[61] D. Pecheur, J. Godlewski, P. Billot, J. Thomazet, Microstructure of oxide films formed during the waterside corrosion of the zircaloy-4 cladding in lithiated environment, in: Zirconium in the Nuclear Industry: Eleventh International Symposium, ASTM International, 1996.

[62] A. Yilmazbayhan, A.T. Motta, R.J. Comstock, G.P. Sabol, B. Lai, Z. Cai, Structure of zirconium alloy oxides formed in pure water studied with synchrotron radiation and optical microscopy: relation to corrosion rate, J. Nucl. Mater. 324 (1) (2004) 6–22.

[63] W. Yang, R. Tucker, B. Cheng, R. Adamson, Precipitates in zircaloy: identification and the effects of irradiation and thermal treatment, J. Nucl. Mater. 138 (2) (1986) 185–195. https://doi.org/10.1016/0022-3115(86)90005-X. http://www.sciencedirect.com/science/article/pii/002231158690005X.

[64] M. Griffiths, R. Gilbert, V. Fidleris, R. Tucker, R. Adamson, Neutron damage in zirconium alloys irradiated at 644 to 710 k, J. Nucl. Mater. 150 (2) (1987) 159–168.

[65] F. Lefebvre, C. Lemaignan, Analysis with heavy ions of the amorphisation under irradiation of zr (fe, cr) 2 precipitates in zircaloy-4, J. Nucl. Mater. 171 (2–3) (1990) 223–229.

[66] D. Pecheur, F. Lefebvre, A. Motta, C. Lemaignan, J. Wadier, Precipitate evolution in the zircaloy-4 oxide layer, J. Nucl. Mater. 189 (3) (1992) 318–332.

[67] Y. Etoh, S. Shimada, Neutron irradiation effects on intermetallic precipitates in zircaloy as a function of fluence, J. Nucl. Mater. 200 (1) (1993) 59–69.

[68] A. Garde, Enhancement of aqueous corrosion of zircaloy-4 due to hydride precipitation at the metal-oxide interface, in: Zirconium in the Nuclear Industry: Ninth International Symposium, ASTM International, 1991.

[69] Y. Nishino, M. Endo, E. Ibe, T. Yasuda, Formation and dissolution of oxide film on zirconium alloys in 288 c pure water under γ-ray irradiation, J. Nucl. Mater. 248 (1997) 292–298.

[70] K. Michel, V. Ozolins, Theory of mass transport in sodium alanate, J. Mater. Chem. 2 (2014) 4438.

[71] G. Eloff, C. Greyling, P. Viljoen, The role of space charge in the oxidation of zircaloy-4 between 350 and 450°c in air, J. Nucl. Mater. 199 (3) (1993) 285–288. https://doi.org/10.1016/0022-3115(93)90149-S. http://www.sciencedirect.com/science/article/pii/002231159390149S.

[72] H.-J. Beie, A. Mitwalsky, F. Garzarolli, H. Ruhmann, H.-J. Sell, Examinations of the corrosion mechanism of zirconium alloys, in: Zirconium in the Nuclear Industry: Tenth International Symposium, ASTM International, 1994.

[73] G.J. Dienes, A. Damask, Radiation enhanced diffusion in solids, J. Appl. Phys. 29 (12) (1958) 1713–1721.

[74] R.S. Averback, H. Hahn, Radiation-enhanced diffusion in amorphous ni-zr alloys, Phys. Rev. B 37 (1988) 10383–10386, https://doi.org/10.1103/PhysRevB.37.10383. https://link.aps.org/doi/10.1103/PhysRevB.37.10383.

[75] J.F. Ziegler, M. Ziegler, J. Biersack, Srim: the stopping and range of ions in matter (2010), nuclear instruments and methods in physics research section B: beam interactions with materials and atoms, in: 19th International Conference on Ion Beam Analysis vol. 268, 2010, pp. 1818–1823 (11), https://doi.org/10.1016/j.nimb.2010.02.091, http://www.sciencedirect.com/science/article/pii/S0168583X10001862.

[76] R. Stoller, M. Toloczko, G. Was, A. Certain, S. Dwaraknath, F. Garner, On the use of srim for computing radiation damage exposure, Nucl. Instrum. Methods Phys. Res. Sect. B Beam Interact. Mater. Atoms 310 (2013) 75–80. https://doi.org/10.1016/j.nimb.2013.05.008. http://www.sciencedirect.com/science/article/pii/S0168583X13005053.

[77] P. Wang, K. Kanjana, D. Bartels, G. Was, In-situ irradiation accelerated oxidation of zircaloy-4 under proton or electron irradiation in pwr primary water, in: 17th International Conference on Environmental Degradation of Materials in Nuclear Power Systems-Water Reactors, vol. 3, 2015, p. 2306.

[78] A. Elliot, Rate Constants and G-Values for the Simulation of the Radiolysis of Light Water over the Range 0-300 Deg C, Tech. Rep., Atomic Energy of Canada Ltd, 1994.

[79] M. Tachibana, K. Ishida, Y. Wada, R. Shimizu, N. Ota, et al., Cathodic polarization properties of hydrogen peroxide and the effect on electrochemical corrosion potential calculation under simulated bwr environment, in: CORROSION 2013, NACE International, 2013.

[80] R. Piotrkowski, A. Denis, J. Kovacs, E. Garcia, Materials interactions during high temperature transients: discussion about the use of the kinetic rate constants in zircaloy oxidation, J. Nucl. Mater. 202 (3) (1993) 252–265.

[81] E. Garcia, G. Béranger, Diffusion model for the oxidation of zircaloy-4 at 400 c in steam. the influence of metallurgical structure (precipitates and grain size), J. Nucl. Mater. 273 (2) (1999) 221–227.

[82] L. J. Siefken, E. W. Coryell, E. A. Harvego, J. K. Hohorst, SCDAP/RELAP5/MOD 3.3 Code Manual, Idaho National Engineering and Environmental Laboratory.

[83] J.P. Pemsler, Diffusion of oxygen in zirconium and its relation to oxidation and corrosion, J. Electrochem. Soc. 105 (6) (1958) 315–322.

[84] B. Cox, J. Pemsler, Diffusion of oxygen in growing zirconia films, J. Nucl. Mater. 28 (1) (1968) 73–78.

[85] F. Garzarolli, H. Seidel, R. Tricot, J. Gros, Oxide growth mechanism on zirconium alloys, in: Zirconium in the Nuclear Industry: Ninth International Symposium, ASTM International, 1991.

[86] B. Ensor, A. Lucente, M. Frederick, J. Sutliff, A. Motta, The role of hydrogen in zirconium alloy corrosion, J. Nucl. Mater. 496 (2017) 301–312.

[87] A. Garner, F. Baxter, P. Frankel, M. Topping, A. Harte, T. Slater, P. Tejland, J. Romero, E. Darby, A. Cole-Baker, et al., Investigating the effect of zirconium oxide microstructure on corrosion performance: a comparison between neutron, proton, and nonirradiated oxides, in: Zirconium in the Nuclear Industry: 18th International Symposium, ASTM International, 2018.

[88] K. Sickafus, H. Matzke, T. Hartmann, K. Yasuda, P.C. J.Valdez III, M. Nastasi, R. Verrall, Radiation damage effects in zirconia, J. Nucl. Mater. 274 (1) (1999) 66–77. https://doi.org/10.1016/S0022-3115(99)00041-0. http://www.sciencedirect.com/science/article/pii/S0022311599000410.

[89] A. Benyagoub, Mechanism of the monoclinic-to-tetragonal phase transition induced in zirconia and hafnia by swift heavy ions, Phys. Rev. B 72 (2005), 094114, https://doi.org/10.1103/PhysRevB.72.094114. https://link.aps.org/doi/10.1103/PhysRevB.72.094114.

[90] P. Platt, E. Polatidis, P. Frankel, M. Klaus, M. Gass, R. Howells, M. Preuss, A study into stress relaxation in oxides formed on zirconium alloys, J. Nucl. Mater. 456 (2015) 415–425. https://doi.org/10.1016/j.jnucmat.2014.09.072. http://www.sciencedirect.com/science/article/pii/S0022311514006722.

[91] R.A. Meserve, J.L. Rempe, Assessment of Missions and Requirements for a New u.S. Test Reactor, 2017. https://www.energy.gov/sites/prod/files/2017/02/f34/NEAC\%20Test\%20Reactor\%20Charge\%20Report\%202-18-17.pdf.